Dalton Transactions

ROYAL SOCIETY OF CHEMISTRY

PAPER

View Article Online
View Journal

Check for updates

Cite this: DOI: 10.1039/d6dt00434b

Co^{2+} ion-doped MnO_2 electrode for microfluidic H_2O_2 biosensors: formation, characterization, and catalytic performance

Veronika Poltavets, *[a,b] Mirosław Krawczyk, [a] Ganna Maslak [b] and
Martin Jönsson-Niedziółka *[a]

Received 18th February 2026,
Accepted 23rd April 2026

DOI: 10.1039/d6dt00434b

rsc.li/dalton

H_2O_2 serves as a vital signalling molecule within biological systems and presents potential as a disease biomarker. Consequently, the development of sensitive and accurate sensors for its measurement within microfluidic systems is of significant importance. This article focuses on the development of a working electrode for an electrochemical microfluidic system designed for the quantitative determination of hydrogen peroxide. Here, we show that a MnO_2-based catalytic material can be improved by adding Co^{2+} ions. By changing the Co^{2+} concentration, an electrode material with improved catalytic performance was formed. The results of amperometric measurements of catalytic activity show a substantial increase in sensitivity and an expanded range of H_2O_2 concentrations that can be quantified using the new electrode. The characteristics of the MnO_2-modified Co^{2+} electrode were thoroughly examined by SEM, XPS. The combination of previously accumulated material and new data offers insights into the underlying reasons for the high catalytic activity of MnO_2, supported by quantum-chemical calculations. This research lays the groundwork for a method utilizing MnO_2 as a working electrode for detecting the concentration of H_2O_2 within a microfluidic cell. During experiments, a stop-flow protocol is employed, enabling data collection from coulometric measurements of the electrochemical processes occurring on the electrode within a limited measurement timeframe.

1. Introduction

Microfluidic systems as an analytical tool are a relatively recent development, but their use opens up great prospects.[1–3] In the development of electrochemical microfluidic biosensors, the formation of working electrodes is of utmost importance. These electrodes should provide sensitivity and selectivity to the sensor, but another important characteristic, especially in microfluidic systems, is mechanical strength.[4–6] Therefore, electrodes with a catalyst layer are developed individually for specific analytes. The aim of this research is to develop a microfluidic biosensor for the determination of H_2O_2 in biological samples. Such sensors are of crucial importance and in high demand for a great number of applications. H_2O_2 is an anchor substance in the body's antioxidant system: peroxide compounds are intermediates or end products in almost all transformations.[7,8] Consequently, H_2O_2 can be used as a marker in biosensors for studying cancer tissue,[9–13] diseases of various organs,[14–17] *etc*. In Ukraine, since the beginning of the war, such studies are unfortunately in demand, in such topics as the influence of polytrauma on the development of oxidative stress in people exposed to blast injuries.

In most studies, Au nanoparticles are used as a catalyst for the detection of H_2O_2,[18–22] and the much cheaper MnO_2 (a specific catalyst for the decomposition of H_2O_2) is used much less frequently.[23,24] In our previous work, we developed an electrode that performed very well for glucose detection in microfluidic systems. This electrode was based on MnO_2 electrochemically deposited on the surface of ITO under conditions selected to exhibit maximum catalytic properties for high selectivity and sensitivity for hydrogen peroxide detection. In this study, we aim to improve the catalytic properties of MnO_2 by doping the oxide with Co^{2+} ions. The method of oxide doping is quite widespread,[25–27] but despite this, there are only a few works on MnO_2 doping with cobalt ions,[28,29] although one might have expected otherwise since the cobalt atom is very close in size to the manganese atom.

Investigating the reasons for the influence of doping on the properties of MnO_2 is also of interest. Most studies agree that doping affects defects in the crystal lattice of MnO_2.[30] We will try to consider this effect from the point of view of changes in

---

[a] *Institute of Physical Chemistry of the Polish Academy of Sciences, Kasprzaka street 44/52, 01-224 Warsaw, Poland. E-mail: verapolt9@gmail.com, mkrawczyk@ichf.edu.pl, martinj@ichf.edu.pl*

[b] *Department of Biochemistry and Medical Chemistry, Dnipro State Medical University, ul. Volodymyr Vernadsky 9, 49044 Dnipro, Ukraine. E-mail: 205_01@dmu.edu.ua*

the oxygen-containing compounds in the sediment composition compared to pure MnO_2. To do this, we use XPS, SEM, and quantum chemical modelling to analyse a set of electrodes characterised by different contents of Co^{2+} ions.

The final part of this research is the creation of a microfluidic chip where the developed electrode was utilised to determine H_2O_2 concentrations.

2. Experimental

2.1. Reagents and chemicals

All materials and chemicals were purchased commercially and used in the form in which they were received. Manganese sulphate, cobalt sulphate and sodium sulphate for electrolytes preparation, sodium dihydrogen phosphate dihydrate and sodium hydrogen phosphate dihydrate for preparation of phosphate buffer (PB) (0.1 M, pH 7), and hydrogen peroxide (30%) were supplied by Sigma Aldrich. All solutions were prepared with ultra-pure water (18.2 MΩ cm) from a Sartorius Arium Comfort I system. ITO-coated glass was obtained from Biotain Crystal Co., Limited, with the following characteristics: resistance 6÷8 Ohm sq^{-1}, ITO coating thickness ∼185 nm, transmittance >84%.

2.2. Fabrication of MnO_2 films on the surface of ITO

Glass substrates were sonicated for 20 min in acetone, then in ethanol, washed with deionised water and dried with an Ar stream. A hole laser cut in Kapton tape defined the working area of the electrode of 0.69 cm^2. The electrochemical formation of the electrodes' functional layer was carried out by the methods of cyclic voltammetry (CV) with the region of scanned potentials from 1.0 V to 1.8 V. As electrolytes, we used water solutions of 0.005 M $MnSO_4$, 0.5 M Na_2SO_4 with pH 1 (the pH was adjusted by adding sulfuric acid) and added $CoSO_4$ in concentrations 0.01 M, 0.05 M and 0.1 M. The scan rate was 50 mV s^{-1}. All electrochemical experiments were performed using a potentiostat/galvanostat BioLogic, model SP-300 in a conventional three-electrode glass cell. An Ag/AgCl/3 M KCl electrode was used as reference and a Pt mesh as counter electrode. Each potential reported in this paper is given against Ag/AgCl/3 M KCl at a laboratory temperature of 25 ± 1 °C. After electrodeposition, the dioxide films were dried at 60 °C or 90 °C in air for 15 h. Initial tests were performed with a Pt working electrode, which is a platinum disk with a diameter of 4 mm sealed in Teflon. The electrode surface was prepared as follows: mechanical polishing, rinsing with deionized water, and oxidation in a "piranha" solution (a mixture of concentrated sulfuric acid and hydrogen peroxide) for 5 min.

2.3. Analytical procedures for determination of H_2O_2

The electrochemical measurements were all carried out at a temperature of 37 °C (the temperature was maintained in a water bath). The cyclic voltammograms of the MnO_2/ITO electrode were scanned from 0.2–0.9 V in 0.1 M PB. The scan rate was 100 mV s^{-1}.

The catalytic activity of the MnO_2/ITO electrodes was determined using chronoamperometry in 0.1 M PB. The amperometric response was measured at an applied potential of 0.45 V *vs.* Ag/AgCl/3 M KCl during repeated injections of hydrogen peroxide.

2.4. Physical characterization of MnO_2/ITO electrodes

The Microstructure and morphology of the MnO_2/ITO samples were investigated using a FEI Nova NanoSEM 450 scanning electron microscope.

Electrochemical impedance spectroscopy (EIS) was measured at OCP in 5 mM $[Fe(CN)_6]^{3-/4-}$ in the frequency range of 0.25 to 100 000 Hz with an amplitude of 5 mV.

X-ray photoelectron spectroscopic (XPS) measurements were performed using a PHI 5000 VersaProbe (ULVAC-PHI) spectrometer with monochromatic Al Kα radiation (h = 1486.6 eV) from an X-ray source operating at 100 μm spot size, 25 W and 15 kV. The high-resolution (HR) XPS spectra were collected with a hemispherical analyser at a pass energy of 117.4 and an energy step size of 0.1 eV. The X-ray beam was incident at the sample surface at an angle of 45° with respect to the surface normal, and the analyser axis was located at 45° with respect to the surface. The CasaXPS software was used to evaluate the XPS data. Deconvolution of all HR XPS spectra was performed using a Shirley background and a Gaussian peak shape with 30% Lorentzian character. The measured binding energies (BE) for individual elements were corrected with respect to the C 1s carbon peak at 284.8 eV.

2.5. Quantum chemical calculations

Quantum chemical modelling was performed using non-empirical methods of the WinGAMESS program.[31–35] Cluster systems were calculated using the spin-unrestricted Hartree–Fock method. The central metal atom was described by the ECP basis, and the ligand atoms by the 6-311G basis. The hybrid B3LYP method of density functional theory was used, which included five functionals: Becke, Slater, and Hartree–Fock exchange functionals, as well as LYP and VWN5 correlation functionals. In the simulation process, the studied ions were optimised in the environment of the first solvation shell and the energies of the optimised complexes were calculated. Then, the energies were refined taking into account solvation using the polarisation continuum model.

Since it makes sense to compare the electronic energies of different structures only if they contain the same type of atoms, when calculating the energy of complexes with different geometries of the first hydrate shell, we considered cluster systems of the composition $[Mn^{z+}(H_2O)_n]\cdot xH_2O$ under the condition that $(n + x)$ = const. In this structure, n water molecules are directly connected to the central atom of the aqua complex, and the remaining x water molecules are at some distance, which excludes their chemical interaction with the metal ions. The cluster structure with the smallest sum of the energies of the metal aqua complex $[Mn^{z+}(H_2O)_n]$ and the energies x of the water molecules moved to the outer sphere was considered to be the most energetically favourable.

2.6. Microfluidic testing. Fabrication of the microfluidic system

The PDMS chip is a T-shaped channel with two inputs. The channels are 250 microns high and 500 microns wide. Fluid manipulations were controlled by a Nemesys pump controlled using dedicated computer software. The PDMS chip was connected to the ITO glass with a 2 mm wide working electrode formed on it and with a graphite counter electrode at a distance of 2 mm from the working electrode. A silver chloride electrode was connected between them as a reference electrode. All measurements were carried out and recorded using a potentiostat, the characteristics of which are given in section 2.2.

3. Results and discussion

3.1. Electrodeposition of doped Co^{2+} MnO_2 on ITO

The formation of precipitates was carried out based on the experience of precipitation of pure manganese dioxide from a sulphate electrolyte (Fig. 1d).

In our previous work[36] the MnO_2 coating with the best catalytic and mechanical properties was formed by cyclic voltammetry (CV) in a solution with pH 1 and subsequently dried at 60 °C for 12 hours. These settings were selected as the starting point for the new electrode formation. The pristine MnO_2 electrode is hereafter referred to as pH1_CV_60 and serves as a reference for comparison with the Co^{2+}-doped samples throughout this study. To obtain precipitates doped with Co^{2+} ions, sulphuric acid electrolytes were prepared with the addition of cobalt sulphate in concentrations from 0.01 M to 0.1 M. The quantities are significant, but it should be taken into account that it is unlikely that positively charged ions will move to the positively charged anode during electrophoresis; most likely, the doping mechanism is somewhat different.

Fig. 1a shows the CV dependence in a solution where only Co^{2+} ions are present. No reaction is observed on the platinum anode, which means that all the Ox-Red reactions in Fig. 1b–d are associated with the oxidation of the Mn^{2+} ions. Fig. 1b and c show the process of MnO_2 coating formation in the presence of 0.01 M and 0.1 M Co^{2+} ions in solutions, respectively. The influence of the doping agent on the deposition process can be analysed by comparison with the dependence in Fig. 1d (precipitation of pure manganese dioxide). We observe a shift in the electrooxidation potential of Mn^{2+} by 0.5 V in the negative direction, which we associate with the influence of Co^{2+} ions. Based on the following studies, it can be assumed that Co^{2+} ions affect the structure and composition of the complex, in which divalent manganese is oxidized at the anode. Perhaps it is as part of such complexes that cobalt is delivered to the surface of the electrode, where it is incorporated into the forming deposit. The impact of cobalt ions on the nucleation and initial stages of manganese dioxide electrodeposition remains a subject of significant interest and warrants further investigation.

For catalytic studies, a set of sediments was prepared using different precipitation conditions. The differences are in the content of cobalt ions in the electrolyte and the number of CV cycles, resulting in different thicknesses of the sediment. The names of the electrodes used in the remainder of the article, with the corresponding deposition conditions, are summarised in Table 1.

3.2. Characterization of electrodes

X-ray photoelectron spectroscopy (XPS) measurements were carried out to determine the presence of Co^{2+} ions in the sediment of MnO_2. We also investigated the influence of the electrolyte composition on the content and composition of the resulting catalysts from the point of view of manganese forms. The following three coatings were selected: 0.01Co_30;

Table 1 Conditions of precipitation formation

	Common conditions of electrodeposition electrolyte: 0.5 M Na_2SO_4, 0.005 M $MnSO_4$, pH1, with the addition of $CoSO_4$	
Name of sample	Concentration of Co^{2+}, M	Number of CV cycles
0.01Co_20	0.01	20
0.01Co_30	0.01	30
0.01Co_40	0.01	40
0.01Co_50	0.01	50
0.05Co_20	0.05	20
0.05Co_30	0.05	30
0.05Co_40	0.05	40
0.05Co_50	0.05	50
0.1Co_20	0.1	20
0.1Co_30	0.1	30
0.1Co_40	0.1	40
0.1Co_50	0.1	50
pH1_CV_60	—	30

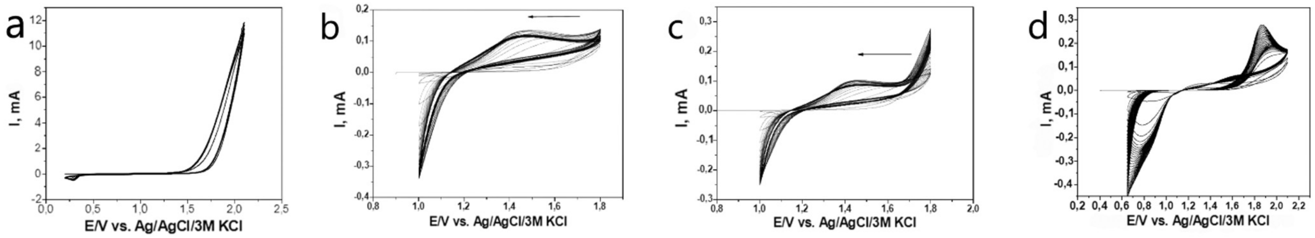

Fig. 1 (a) CV obtained by polarizing the Pt electrode in an electrolyte of the composition 0.5 M Na_2SO_4 + 0.1 M $CoSO_4$, pH1; electrodeposition of MnO_2 by CV method from solution of 0.005 M $MnSO_4$ + 0.5 M Na_2SO_4 electrolyte, pH1 in the presence of (b) 0.01 M $CoSO_4$, (c) 0.1 M $CoSO_4$, (d) without additives. Scan rate 50 mV s^{-1}.

0.05Co_30; 0.1Co_30 (the description of precipitation formation is given in section 3.1). The composition of electrolytes differed only in the concentration of cobalt ions.

The obtained XPS spectra are shown in Fig. 2. We used studies[37–40] that provide detailed descriptions of the interpretation of the XPS spectra of MnO_2 sediments. The Mn 2p spectrum provides information that we indeed have a precipitate of manganese dioxide through the value of spin energy separation, which is equal to the distance between the Mn $2p_{3/2}$ and Mn $2p_{1/2}$ signals. The areas of the peaks at 641.9 eV and 644.9 eV of the Mn $2p_{3/2}$ signal allow us to calculate the ratio of the Mn^{3+} and Mn^{4+} forms. Particularly interesting results were obtained from the analysis of the O 1s spectrum. We identify the peak at 529.6 eV as the presence of Mn–O–Mn bonds, and the peak at 531.3 eV corresponds to the presence of Mn–O–H bonds. The Co 2p2 spectrum confirms the presence of Co^{2+} ions in the resulting precipitates. The amount of cobalt ions we present as the content in the sediment relative to all manganese ions. The results are given in Table 2. We also added the results of XPS analysis of pure MnO_2, which was de-

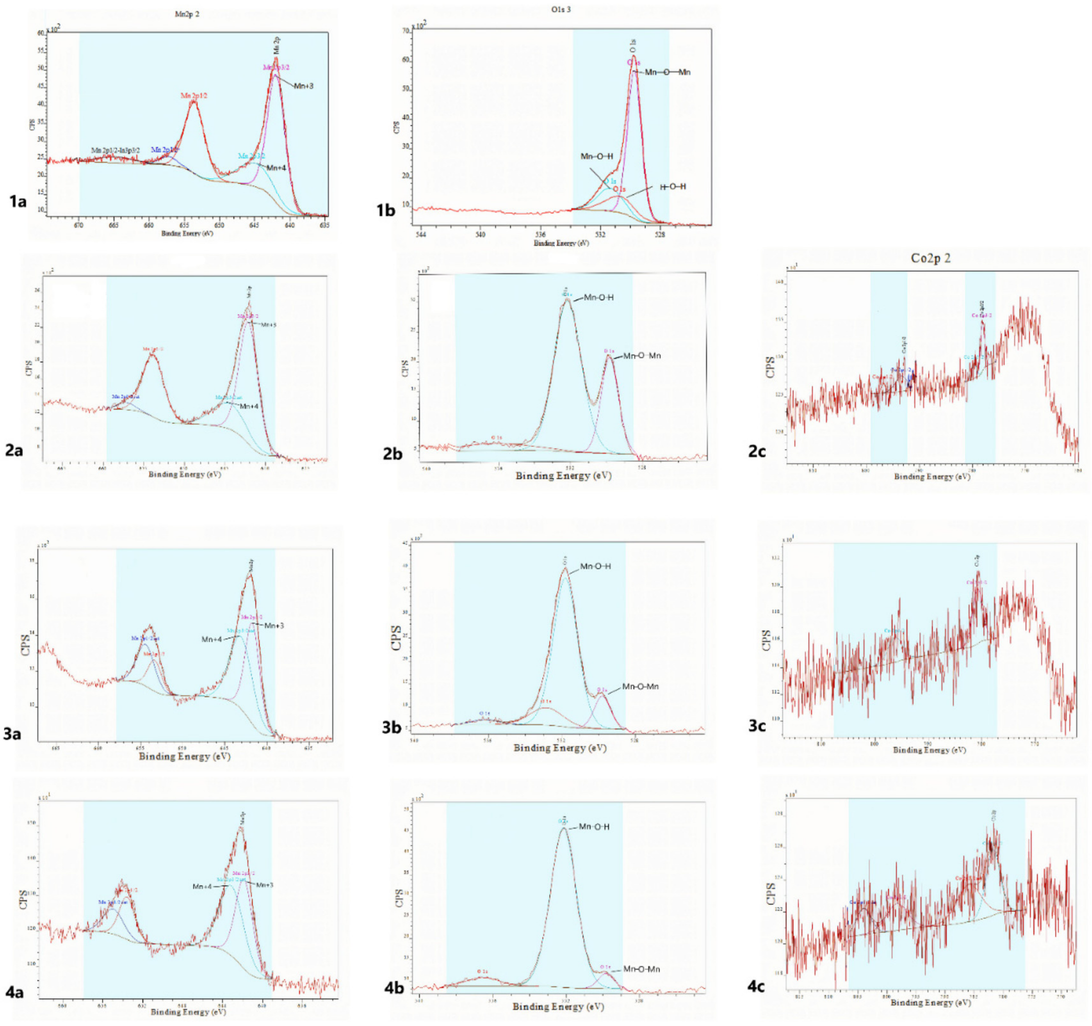

Fig. 2 Mn 2p, O 1s, Co 2p XPS spectra of (**1a**, **1b**) pH1_CV_60; (**2a**, **2b**, **2c**) 0.01Co_30; (**3a**, **3b**, **3c**) 0.05Co_30; (**4a**, **4b**, **4c**) 0.1Co_30. For details, see the main text.

Table 2 The XPS spectra interpretation

Precipitate	Mn 2p spectrum, spin energy separation, eV	Mn^{3+}, %	Mn^{4+}, %	Mn–O–Mn, %	Mn–O–H, %	Co^{2+}, %
Pristine MnO_2 (pH1_CV_60)	11.7	67.9	32.09	65.53	18.62	—
0.01Co_30	11.7	47	52.9	26.23	65.68	2.3
0.05Co_30	11.6	63.9	36	10.99	74.36	2.4
0.1Co_30	11.8	54.3	45.7	4.95	88.84	6.8

posited under the same conditions. This way we can see the effect of doping on the catalyst composition.

For reference, data for the pristine MnO_2 electrode (labelled 'pH1_CV_60' in section 3.1) are included. From the data in the table, we can conclude that Co^{2+} ions are indeed present in the structure of the formed MnO_2-based coating. However, their content does not linearly depend on the concentration in the solution. We see a sharp increase at 0.1 M Co^{2+} concentration in the electrolyte.

The ratio of Mn^{3+}/Mn^{4+} forms changes in the direction of increasing the content of manganese in its tetravalent form. The increase in catalytic activity due to the increase in the Mn^{4+} content agrees with the conclusions from our previous publication.[36] Also, the data shows that with the addition of Co^{2+} ions into the sediment, the amount of Mn–O–H bonds increases sharply. Such significant changes in the sediment composition can also influence the increase in the catalytic activity of the electrodes.

Electrochemical impedance spectroscopy (EIS) was performed on selected samples, with the corresponding data and parameters provided in Fig. 3 and Table 3, respectively.

Charge transfer kinetics within the film were elucidated using the $R_1 + Q_2/(R_2 + W_2)$ equivalent circuit. The parameters include uncompensated resistance R_1, charge-transfer resistance R_2, a constant phase element Q_2, and the Warburg impedance W_2.

A comparative analysis of the data presented in Fig. 3 and Table 3 reveals a clear correlation between the electrode composition and its electrochemical properties. For reference, data for the pristine MnO_2 electrode (labelled 'pH1_CV_60' in section 3.1) are included. As shown in Table 2, an increase in the Co^{2+} dopant concentration leads to a significant reduction in electrode conductivity. This trend is attributed to the formation of the MnOOH phase during the doping process, as indirectly supported by the XPS analysis. Furthermore, comparing samples 0.1Co_30 and 0.1Co_50 shows that increasing the film thickness further diminishes conductivity, which is expected to influence the subsequent electrocatalytic performance.

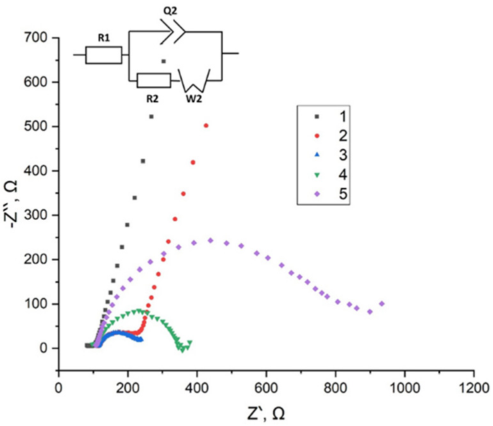

Fig. 3 Electrochemical impedance spectroscopy was performed on the (1) pH1_CV_60, (2) 0.01Co_30, (3) 0.05Co_30, (4) 0.01Co_30, (5) 0.01Co_50. For details, see main text.

The morphology of the sediments were studied by scanning electron microscopy. Fig. 4 shows precipitates doped with Co^{2+}, electrodeposited in solutions with different cobalt ion contents. Fig. 4g and h show the morphology of pure MnO_2 and are given for comparison. All precipitates were formed during 30 cycles of CV at the same pH of the electrolyte and the same concentration of Mn^{2+} ions.

First of all, it is clear that the doped coatings are very similar. The structure is branched like the branches of trees. When compared with pure MnO_2, the structure is more branched, but the branches are smaller. We also observe an increase in the density of sediments; the structure of the ITO is not visible through the layer of manganese dioxide. At lower magnification we note the uniformity of the coating. We observe the integrity of the sediment, there are no cracks, which was typical for pure MnO_2. As was the case with pure MnO_2, XRD (SI) shows that the deposited film is amorphous, without clear peaks from manganese oxide.[36]

When cobalt ions are added to the electrolyte, the resulting deposits become much denser, but the structure remains branched. The composition of the coating has undergone significant changes. The ions Co^{2+} were found in the structure of all sediments. The effect on the structure of MnO_2 is also noticeable: the number of hydroxyl groups associated with manganese has sharply increased (Mn–O–H bonds).

3.3. Analytical procedure for the determination of H_2O_2

Based on convincing data from the literature,[41,42] the mechanism of formation of an electrochemical signal during anodic polarisation of the working electrode is as follows. H_2O_2 decomposes into water and molecular oxygen when it comes into contact with MnO_2. The catalytic action is exerted by Mn^{4+}, which is reduced to Mn^{3+}. During anodic polarisation of the electrode, the Mn^{3+} will be electrochemically oxidized back to Mn^{4+}, which can be measured as a faradaic current. Interpretation of the data from the catalytic studies will be grounded in this theory.

The catalytic effect of the precipitate and the potentials at which it is observed were investigated by comparing voltammograms recorded in the presence and absence of H_2O_2 (Fig. 5). The cyclic voltammograms in the presence of H_2O_2 (Fig. 5(2)) show a higher current than CVs in the absence of

Table 3 The values of charge-transfer resistance, R_2, for the corresponding precipitation in Fig. 3

Electrode	Pristine MnO_2 (pH1_CV_60) (1)	0.01Co_30 (2)	0.05Co_30 (3)	0.1Co_30 (4)	0.1Co_50 (5)
R_2, Ohm	87.11	123.8	131.1	238.2	708.6

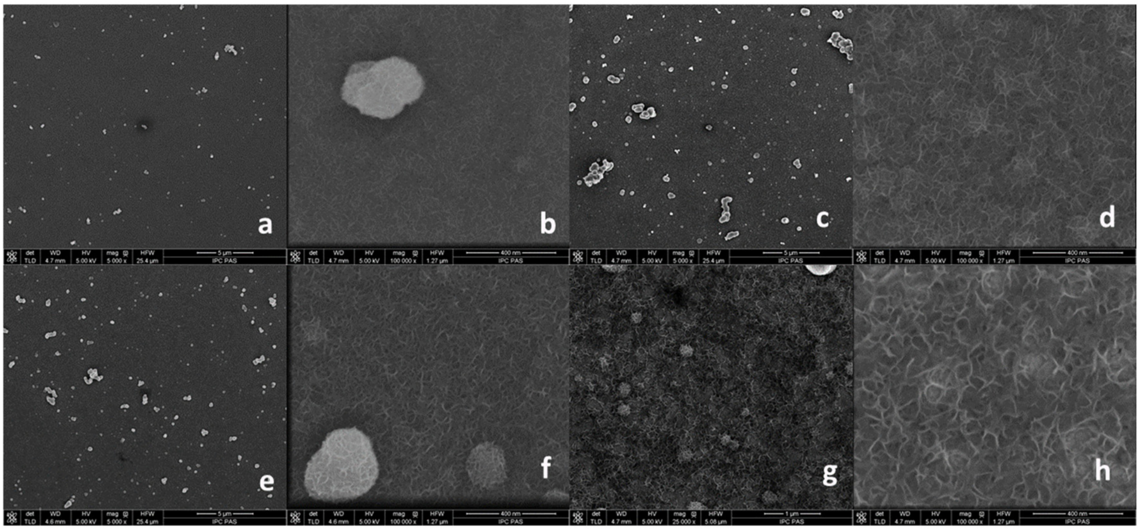

Fig. 4 SEM images of MnO_2 films deposited under conditions: (a and b) 0.01Co_30, (c and d) 0.05Co_30, (e and f) 0.1Co_30, (g, h) pH1_CV_60. For details, see the main text.

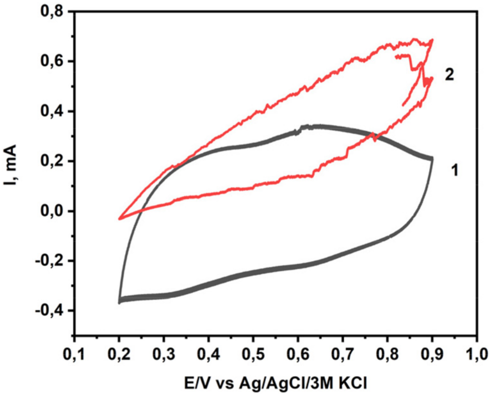

Fig. 5 CVs of electrode 0.1Co_30 in the absence (1) and presence (2) of 2 mM H_2O_2 in PB. Scan rate 100 mV s^{-1}.

hydrogen peroxide (Fig. 5(1)) even at low potentials. This means that even a low anodic polarisation will provide an analytical signal.

Chronoamperometry was chosen as the main method for studying the catalytic activity in determining H_2O_2 for a set of 12 electrodes. The method is indicative and convenient in interpretation. 0.45 V *vs.* Ag/AgCl/3 M KCl was chosen as a favourable potential at which the analytical signal is recorded. At this potential, we record sufficient catalytic activity, but avoid excess noise from the evolved gaseous products. Additionally, low values of electrode polarisation are desirable when studying biological objects, due to the presence of potentially interfering reactions.

Fig. 6 shows the *I*–*t* dependences of all electrodes with H_2O_2 injections in such a way that the concentration of peroxide in the electrolyte changes stepwise according to the following scheme: 0.1 mM → 0.2 mM → 0.5 mM → 1 mM → 2 mM → 3 mM → ··· → n mM. The high level of noise seen in Fig. 5 is due to the release of gaseous products from the decomposition of H_2O_2 while testing the electrodes, as described above.

For clarity, the results are divided into three groups: each Fig. 6a, b and c shows chronoamperograms of electrodes formed with the same concentration of Co^{2+} ions and differ in

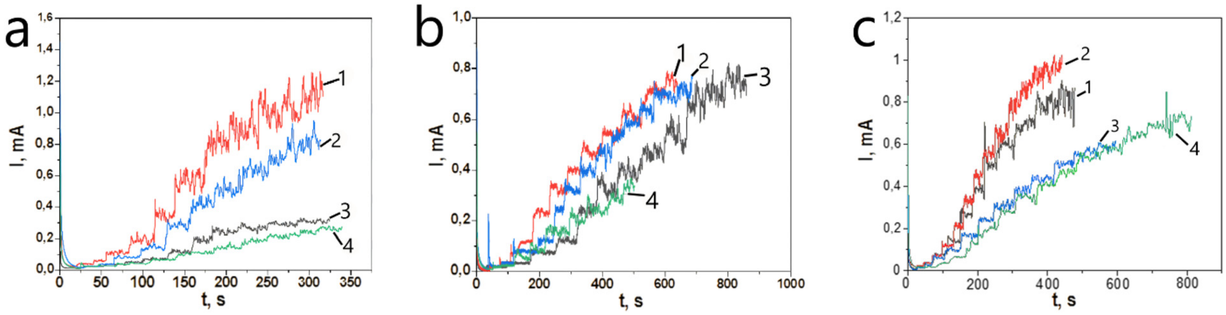

Fig. 6 Amperometric *I*–*t* curveson successive injection of H_2O_2 into the stirring PB at the applied potential of 0.45 V *vs.* Ag/AgCl/3 M KCl of MnO_2 dopped with Co^{2+} electrodes: (a1) 0.01Co_20, (a2) 0.01Co_30, (a3) 0.01Co_40, (a4) 0.01Co_50, (b1) 0.05Co_20, (b2) 0.05Co_30, (b3) 0.05Co_40, (b4) 0.05Co_50, (c1) 0.1Co_20, (c2) 0.1Co_30, (c3) 0.1Co_40, (c4) 0.1Co_50. Note that vertical scales are different.

sediment thickness. Thus, it is immediately clear that electrodes deposited with 20 to 30 CV cycles exhibit the highest activity. The activity of the catalysts decreases sharply at 40 and 50 CV cycles. This decrease in MnO_2 catalytic activity is a consequence of the relatively poor electrical conductivity of the material The *I*–*t* dependencies of the best representatives of each group are converted into an amperometric response to H_2O_2 concentration and are compared with each other and with a pristine MnO_2 electrode (labelled 'pH1_CV_60' in section 3.1) (Fig. 7).

All catalysts doped with Co^{2+} ions show a sharp increase in the range of detectable H_2O_2 concentrations compared to pure MnO_2.

Another important parameter of such a dependence is its linearity. In this case, we have a calibration plot of electrocatalytic current *versus* H_2O_2 concentration. Pure MnO_2 shows a linear relationship with the concentration of H_2O_2 from 0.1 mM to 3 mM. Electrode 0.01Co_20 – from 0.1 mM to 4 mM, electrode 0.05Co_30 – from 0.1 mM to 6 mM, electrode 0.1Co_30 – from 0.1 mM to 9 mM. When selecting the electrode with the best performance, we distinguish 0.1Co_30 with the widest range of the calibration plot. Such a great improvement in the catalytic properties of the sediment, from the point of view of all the above studies, can be associated with a sharp increase in the Mn–O–H groups and their participation in the decomposition of hydrogen peroxide. We are going to consider changes in the electrode structure during the electrode transition. For this, we use the capabilities of quantum chemical modelling.

3.4. Quantum chemical computations

The purpose of the calculations was to study the oxidation reaction of Mn^{3+} to Mn^{4+}, which is responsible for the electrocatalysis of the material. Section 2.5 provides references showing good correlation between calculated data and experimental data for Mn complexes.

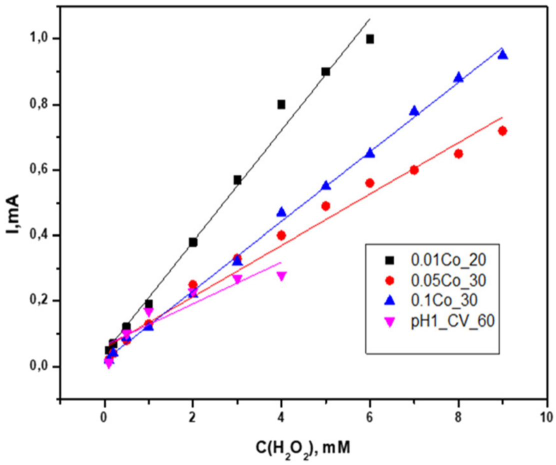

Fig. 7 Relationship of the amperometric response *vs.* the H_2O_2 concentration.

As is known from previous studies,[43] manganese dioxide contains Mn^{3+} in hydrolysed form. It is in these forms that we find the presence of the Mn–O–H bonds that attracted attention in the XPS study. All possible clusters were analysed and the actual charge distributions in them were calculated, and the spatial particles were constructed. The results are shown in Table 4.

From Table 4, which shows the charge levels in trivalent manganese complexes, we can conclude that in reality, the Manganese atom does not carry a charge of +3, but rather the charge is redistributed among the oxygen-containing clusters around the central atom. Therefore, the hydrolysed form of Mn^{3+} is natural. And it is precisely in such complexes that a large presence of Mn–O–H bonds is observed.

The next stage of calculations is the analysis of energy changes associated with the transition of an electron during the oxidation of trivalent manganese to the tetravalent state and back. This is actually the reaction that provides electrocatalysis. Possible reactions of electron transition from hydrolysed trivalent manganese are presented in Table 5. There you can see the energy characteristics of electron transition and the calculated standard electrode potentials of these reactions.

Most likely reaction number 5 occurs. The standard electrode transition potential is very low, which correlates with our catalytic measurements. We conclude that trivalent manganese in the electrolytic film MnO_x is present in the form of the compound $[MnO(OH)(H_2O)_2]$. Removing water and the OH group from the structure showed that such a particle could not be calculated, which demonstrates the importance of the presence of these groups in the structure of the sediment. Calculations also indicate that other particle geometries are possible, but the electrode transition potential increases sharply in this case. In Fig. 8 shows the structures of $[MnO(OH)(H_2O)_2]$ in the original and, accordingly, in the oxidized state.

As can be seen, the removal of an electron from $[MnO(OH)(H_2O)_2]$ does not lead to a significant reorganization of its structure. The Mn–OH bonds remain unchanged and stable: the internuclear distances in them are 1.99 Å and 2.01 Å in the molecular form and 1.99 Å and 1.99 Å in the ionized form. A slight displacement of Manganese and Oxygen nuclei is observed only in Mn–O and Mn–O–H bonds. In the molecular form, they are 1.73 Å and 1.88 Å, respectively, and in the ionized form, 1.65 Å and 1.74 Å. The valence angle O–Mn–O–H

Table 4 Distribution of charges on manganese atoms and ligands in clusters $[Mn\ (OH)_x(H_2O)_n]^{z+}\ (H_2O)_m$ and $[Mn\ O(OH)(H_2O)_2] + (H_2O)_2$

Clusters	q(Mn)	$q(\sum OH)$	q(O)	$q(\sum H_2O)$
$[Mn(OH)(H_2O)_5]^{2+}$	+1937	−0362	—	+0425
$[Mn(OH)_2(H_2O)_4]^{+}$	+1751	−0996	—	+0244
$[Mn(OH)_3(H_2O)_2]^{0}(H_2O)$	+1500	−1607	—	+0127
$[MnO(OH)(H_2O)_2]^{0}(H_2O)_2$	+1342	−0561	−0829	+0048
$[Mn(OH)(H_2O)_5]^{3+}$	+2121	+0076	—	+0801
$[Mn(OH)_2(H_2O)_4]^{2+}$	+1819	−0341	—	+0522
$[Mn(OH)_3(H_2O)_2]^{+}(H_2O)$	+1589	−0832	—	+0244
$[MnO(OH)(H_2O)_2]^{+}(H_2O)_2$	+1617	−0414	−0469	+0266

Table 5 Values of standard Red-Ox potentials of one-electron oxidation of hydrolysed forms of manganese(III) aquacomplexes

No.	Reaction	ΔE, kJ mol^{-1}	φ^0, V (standard hydrogen potential)
1	$[Mn(OH)(H_2O)_5]^{2+} = [Mn(OH)(H_2O)_5]^{3+} + e$	775 791	2.90
2	$[Mn(OH)_2(H_2O)_4]^{+} = [Mn(OH)_2(H_2O)_4]^{2+} + e$	692 902	2.15
3	$[Mn(OH)_3(H_2O)_3]^{0} = [Mn(OH)_3(H_2O)_2]^{+}(H_2O) + e$	577 246	1.11
4	$[Mn(OH)_3(H_2O)_2]^{0}(H_2O) = [Mn(OH)_3(H_2O)_2]^{+}(H_2O) + e$	602 132	1.33
5	$[MnO(OH)(H_2O)_2]^{0}(H_2O)_2 = [MnO(OH)(H_2O)_2]^{+}(H_2O)_2 + e$	512 457	0.53

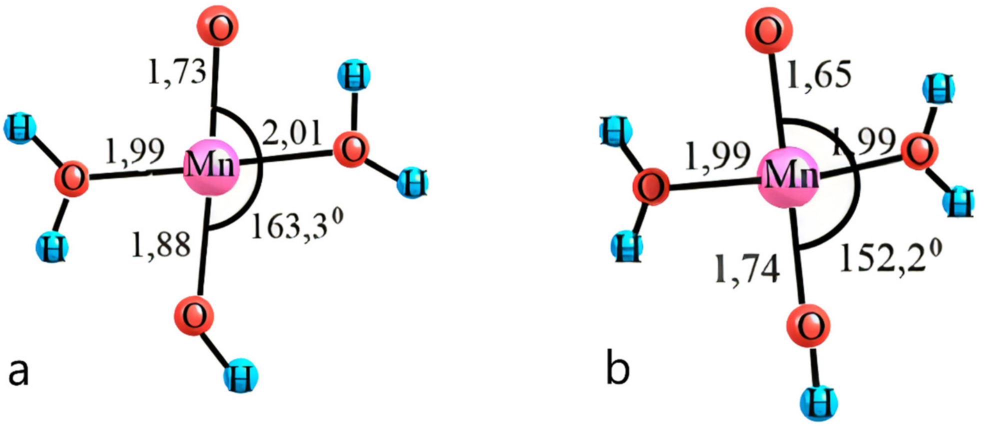

Fig. 8 Spatial structure of particles: a – $[MnO(OH)(H_2O)_2]^0$; b – $[MnO(OH)(H_2O)_2]^+$.

also changes little: from 163.30 in the molecular form to 152.20 in the ionized form. The above listed indicates the absence of major structural and chemical transformations in the redox system $[MnO(OH)(H_2O)_2]/[MnO(OH)(H_2O)_2]^+$. Which makes it possible to use in objects in which rapid charge cycling is assumed.

Thus, it can be concluded that the more Mn–O–H bonds present in the precipitate, the greater the probability of the formation of a hydrolysed structure of trivalent manganese $[MnO(OH)(H_2O)_2]$ a certain geometry. Then the reactions of the Mn^{3+}/Mn^{4+} transformations will occur easily and quickly at minimal electrode polarization potentials. This is reflected in the excellent catalytic performance of the MnO_2 electrode.

3.5. Measurements in a microfluidic system

The developed MnO_2-based electrode with the best performance was implemented as a working electrode in an amperometric microfluidic device for determining the concentration of H_2O_2 in a solution. The creation of the microfluidic cell is described in detail in section 2.6 and is also visually represented in the Fig. 9. The T-shaped channels and two inlets allow manipulation with two working solutions. One of them was PB with H_2O_2 of a given concentration, and the second was pure PB, which was used to wash the channels between receiving signals. In this system, with a very small working electrode area and microamounts of electrolyte, the amplification of the analytical signal is achieved due to the hydrodynamic effect of analyte delivery. H_2O_2 concentrations of the order of µM were measured. However, one drawback of the electrode was noticed. Despite the low speed of liquid movement (20 µl s^{-1}), the MnO_2 layer was quickly washed off during measurements. This is because Mn^{3+} compounds are soluble in water. Thus, despite the high sensitivity, the signal would not reach a steady-state, and a calibration curve could not be established.

Therefore, an alternative scheme for working with MnO_2 electrodes needed to be developed. We stop the flow of electrolyte with H_2O_2 when it hits the electrode and measure the charge (q) passing through the electrode while hydrogen peroxide decomposes. This charge is related to the amount of decomposed H_2O_2 through Faraday's first law:

$$m = M \times q/F \times n,$$

where m is the mass of the manganese that took part in the Ox-Red reaction, proportional to the decomposed hydrogen peroxide, M is the molar mass manganese dioxide, q is the total electric charge passed through the electrolyte (in Coulombs), n is the number of electrons involved in the reaction and F is Faraday's constant, approximately 96 485 Coulombs per mol.

For specific electrolysis M, F, n are constants; thus, the value of q is equivalent to m. In the case of constant-current electrolysis,

$$q = It$$

where I is the current, t is the time of process.

The Fig. 10 shows the signal that we received. The PB solution flows through the channel to point 1. From point 1 to point 2 a solution containing hydrogen peroxide flows. From point 2 to point 3, the movement of solutions in the system stops. From point 3, pure PB flows and washes the cell chan-

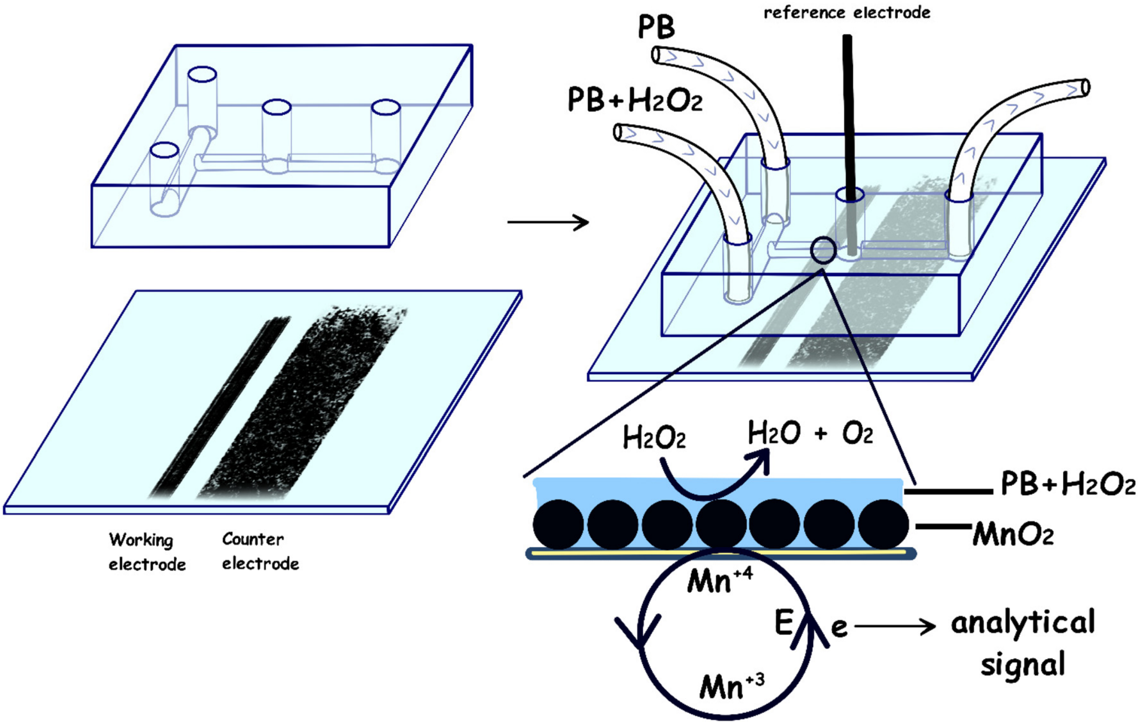

Fig. 9 Microfluidic cell with MnO_2-based working electrode in work.

nels, and the process can be repeated. The charge (q) is measured as the area under the chronoamperogram curve from point 2 to point 3.

Based on our experience, time periods should be selected in accordance with the object of study. In this investigation, the optimal program was as follows: PB flow for 200 s, then inclusion of H_2O_2 in phosphate buffer for 30 s, stopping the flow for the reaction to proceed for 300 s. The flow rate is always 20 µl s^{-1}. In the process of developing the methodology, 4 electrodes were used and 6 concentrations of hydrogen peroxide were measured on them: 5 µM, 10 µM, 15 µM, 20 µM, 30 µM, 40 µM. As a result, calibration curves are considered as the dependence of the charge recorded on the working electrode on the concentration of H_2O_2.

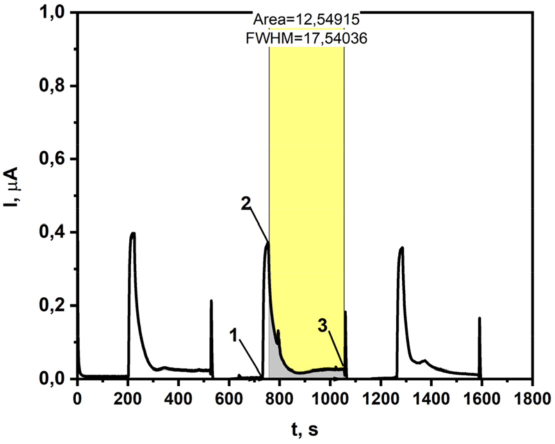

Fig. 10 *I*–*t* dependence obtained in the microfluidic system. Analyte 20 µM H_2O_2 in 0.1 M PB.

The electrodes were evaluated in terms of the reproducibility of successive measurements on them. Referring to Fig. 10, then the first measurement spans from 200 s to 500 s, the second measurement is from 750 s to 1050 s, and the third measurement is from 1300 s to 1600 s. Results for one of the electrodes are shown in Fig. 11. The first measurement can often be unreproducible as shown by a large variation and missing data points. Dependencies 2 and 3 are quite reproducible and have a correlation coefficient of about 0.99. When processing the results. For this reason, the second measurement was used in the analyses.

Fig. 12 shows the calibration curves for four electrodes. Several series of measurements (6 concentrations of hydrogen peroxide) were carried out on all electrodes; the figure shows an example of two series of measurements for the fourth electrode.

All electrodes showed the possibility of constructing a calibration curve with a correlation coefficient from 0.96 to 0.99. However, we note that the reproducibility between electrodes is insufficient. In effect, this means that before using the electrode, a separate calibration should be carried out. But, as the examples 4_1 and 4_2 show, very high reproducibility is seen from measurement to measurement, which implies that this is a manufacturing issue, rather than a fundamental limitation of the MnO_2 electrodes.

This study showed that a highly sensitive electrode for a microfluidic cell was developed for quantitative measurement of H_2O_2 at concentrations as low as 5 µM.

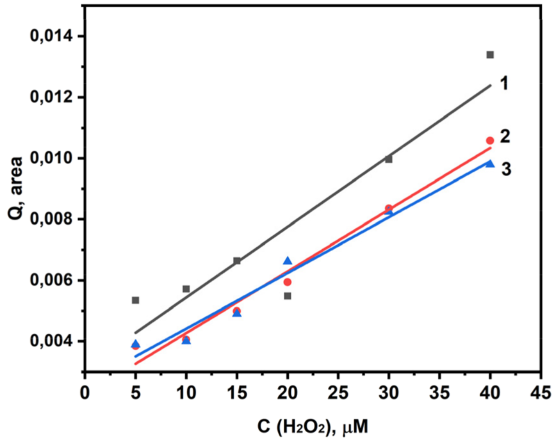

Fig. 11 Dependence of charge recorded on the working electrode on the concentration of H_2O_2: 1 – first measurement, 2 – second measurement, 3 – third measurement.

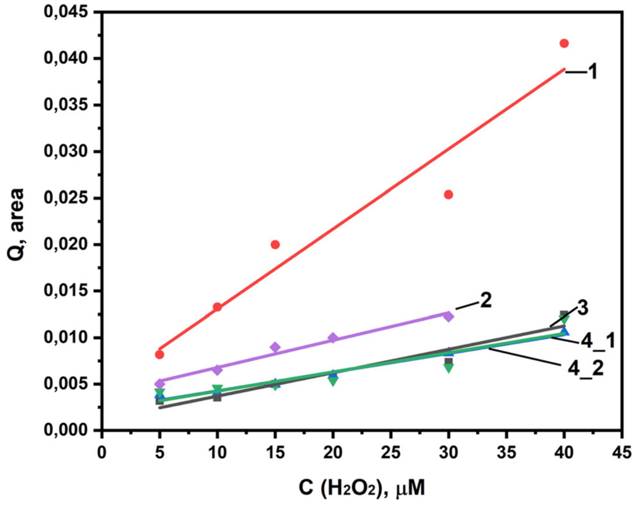

Fig. 12 Dependence of charge recorded on the working electrode on the concentration of H_2O_2: 1 – first electrode, 2 – second electrode, 3 – third electrode, 4_1 –first measurements on the fourth electrode, 4_2 – second measurements on the fourth electrode.

The proposed MnO_2 electrode may exhibit cross-sensitivity to common interferents (*e.g.*, ascorbic and uric acids), potentially compromising its performance in clinical settings. To ensure selectivity in such a case, either mathematical compensation or a Nafion permselective membrane can be employed. The latter acts as a size-exclusion barrier, preventing larger molecules from reaching the electrode surface while allowing the diffusion of H_2O_2.[44]

4. Conclusion

Doping MnO_2 with Co^{2+} ions is a simple procedure, but it significantly improves the catalytic properties of this catalyst. We combined physical methods for studying the composition of sediments and their morphology with quantum chemical modelling of the basic catalytic reaction. The results indicate that due to the increase in the hydrolysed forms of manganese (Mn–O–H bonds), the range of determination of H_2O_2 concentrations relative to pure MnO_2 increases several times. In systematic catalytic studies in a macroscopic cell with stirred solution, the electrode 0.1Co_30 with the highest content of Co^{2+} ions and Mn–O–H bonds in the composition showed mechanical strength, a stable range of determination of hydrogen peroxide concentrations from 0.1 mM to 9 mM. For comparison, the range of detectable H_2O_2 concentrations when using an electrode with pure MnO_2 is from 0.1 mM to 3 mM.

Testing the 0.1Co_30 sample with the best characteristics in a microfluidic system showed the high sensitivity of the catalyst. Stable determination of H_2O_2 concentration 5 μM. The measurement mechanism we have developed takes into account the characteristics of the electrode composition to ensure stability of the electrode during repeated measurements and ensures sufficiently long-term operation with a large number of analysed samples.

We would like to add that after use the MnO_2 layer is easily removed and the ITO base can be used again. Our experience shows that ITO glass can be use this way for at least 6 months with a reprecipitation frequency of once every 1–2 weeks. This makes the analysis inexpensive and environmentally friendly.

Author contributions

VP: conceptualization, formal analysis, investigation (electrochemical experiments), writing – original draft; MK investigation (XPS); GM: investigation (calculations); MJN: formal analysis, funding acquisition, writing – review & editing.

Conflicts of interest

There are no conflicts to declare.

Data availability

Data associated with this paper have been made available at the RepOD repository, https://doi.org/10.18150/PUHR5I.[45]

Supplementary information (SI) is available. See DOI: https://doi.org/10.1039/d6dt00434b.

Acknowledgements

This work was supported by the Norway Grants 2014–2021 *via* the National Centre for Research and Development (NOR/POLNOR/UPTURN_UA/0060/2019).

References

1 D. Zhang, S. Jia, Z. Jin, J. Bu, G. Guo, J. Deng and X. Wang, *ChemElectroChem*, 2025, **12**, e202400666.

2 R. Mohammadi, S. Stavrakis and A. J. deMello, *Adv. Drug Delivery Rev.*, 2026, **232**, 115818.

3 V. Mazzaracchio and F. Arduini, *Anal. Bioanal. Chem.*, 2026, **418**, 459–481.

4 L. Qiang, S. Vaddiraju, J. F. Rusling and F. Papadimitrakopoulos, *Biosens. Bioelectron.*, 2010, **26**, 682–688.

5 S. Kang and J. J. Davis, *Chem. Sci.*, 2025, **16**, 6965–6974.

6 J. Y. Lu, Z. Q. Bu, Y. Q. Lei, D. Wang, B. He, J. Wang and W. T. Huang, *J. Mol. Liq.*, 2024, **409**, 125503.

7 Q.-D. Tai, Y. Tang, S.-T. Xie, Y.-Y. Ye, X. Tang, Q. Lyu, Z.-J. Fan and Y.-H. Liao, *Mater. Today Bio*, 2025, **35**, 102405.

8 E. A. Veal, A. M. Day and B. A. Morgan, *Mol. Cell*, 2007, **26**, 1–14.

9 A. S. Sujitha, M. R. Aswathy, L. Ragupathy and D. Painuly, *Sens. Actuators, B*, 2025, **426**, 137078.

10 S. E. Z. Jawad, S. Ahmed, D. Hussain, J. Najeeb, A. Alam, M. Najam-ul-Haq and B. Fatima, *Sci. Rep.*, 2025, **15**, 237.

11 T. Ali, D. Li, T. N. F. Ponnamperumage, A. K. Peterson, J. Pandey, K. Fatima, J. Brzezinski, J. A. R. Jakusz, H. Gao, G. E. Koelsch, D. S. Murugan and X. Peng, *Cancers*, 2024, **16**, 2171.

12 H. Kacem, L. Kunz, P. Korysko, J. Ollivier, P. Tsoutsou, A. Martinotti, V. Rieker, J. Bateman, W. Farabolini, G. Baldacchino, B. W. Loo, C. L. Limoli, M. Dosanjh, R. Corsini and M.-C. Vozenin, *Radiother. Oncol.*, 2025, **209**, 110942.

13 T. Ahmad, A. Iqbal, S. A. Halim, J. Uddin, A. Khan, S. El Deeb and A. Al-Harrasi, *Nanomaterials*, 2022, **12**, 1475.

14 J. D. La Favor and A. L. Burnett, *Methods*, 2016, **109**, 131–140.

15 J. Pravda, *Mol. Med.*, 2020, **26**, 41.

16 C. Huang, J. Xu, J. Li, S. He, H. Xu, X. Ren, V. Singh, L. Wu and J. Zhang, *Carbohydr. Polym.*, 2022, **285**, 119252.

17 Y. Song, N. Driessens, M. Costa, X. De Deken, V. Detours, B. Corvilain, C. Maenhaut, F. Miot, J. Van Sande, M.-C. Many and J. E. Dumont, *J. Clin. Endocrinol. Metab.*, 2007, **92**, 3764–3773.

18 S. Guo, D. Wen, S. Dong and E. Wang, *Talanta*, 2009, **77**, 1510–1517.

19 W. Dong, Y. Ren, Z. Bai, Y. Yang and Q. Chen, *Bioelectrochemistry*, 2019, **128**, 274–282.

20 M. Delvaux, A. Walcarius and S. Demoustier-Champagne, *Anal. Chim. Acta*, 2004, **525**, 221–230.

21 W. He, Y.-T. Zhou, W. G. Wamer, X. Hu, X. Wu, Z. Zheng, M. D. Boudreau and J.-J. Yin, *Biomaterials*, 2013, **34**, 765–773.

22 Y. Sun, R. Wang, X. Liu, G. Shan, Y. Chen, T. Tong and Y. Liu, *Microchim. Acta*, 2018, **185**, 445.

23 Y. Ye, X. Sun, Y. Zhang, X. Han and X. Sun, *Biosens. Bioelectron.*, 2022, **202**, 113990.

24 L. Li, Z. Du, S. Liu, Q. Hao, Y. Wang, Q. Li and T. Wang, *Talanta*, 2010, **82**, 1637–1641.

25 B. Uddin, Md. O. Farque, Md. Moniruzzaman, Md. J. Uddin, Md. K. Hossain and S. H. Begum, *Chem. Phys. Impact*, 2025, **10**, 100798.

26 T. D. Thanh, D. H. Manh, L. T. H. Phong, T. N. Bach, P. H. Nam, N. T. N. Anh, V. H. Ky, N. T. H. Le and T. M. Thi, *Ceram. Int.*, 2025, **51**, 1448–1455.

27 F. Asaldoust, K. Mabhouti, A. Jafari and M. Taleb-Abbasi, *Sci. Rep.*, 2025, **15**, 1088.

28 C. Xian, R. He, Q. Chen, Q. Li, Y. Ma, S. Bao, W. Sun, H. Chen and M. Xu, *Chem. Eng. J.*, 2025, **512**, 162576.

29 X. Chen, Z. Xu, S. Guo, B. Sun, Q. Li, Q. Meng, F. Wei, J. Qi, Y. Sui and P. Cao, *ACS Appl. Mater. Interfaces*, 2025, **17**, 12074–12084.

30 L. Zudina, G. Sokolsky, V. Chumak and N. Haiuk, *Mater. Today: Proc.*, 2022, **62**, 7759–7766.

31 V. A. Seredyuk and V. F. Vargalyuk, *Russ. J. Electrochem.*, 2008, **44**, 1105–1112.

32 M. W. Schmidt, K. K. Baldridge, J. A. Boatz, S. T. Elbert, M. S. Gordon, J. H. Jensen, S. Koseki, N. Matsunaga, K. A. Nguyen, S. Su, T. L. Windus, M. Dupuis and J. A. Montgomery, *J. Comput. Chem.*, 1993, **14**, 1347–1363.

33 M. Szafran, M. M. Karelson, A. R. Katritzky, J. Koput and M. C. Zerner, *J. Comput. Chem.*, 1993, **14**, 371–377.

34 H. Sakiyama, M. Oshima, S. Suzuki and Y. Nishida, *J. Comput. Chem., Jpn.*, 2009, **8**, 87–92.

35 R. Cammi and J. Tomasi, *J. Comput. Chem.*, 1995, **16**, 1449–1458.

36 V. Poltavets, M. Krawczyk, G. Maslak, O. Abraimova and M. Jönsson-Niedziółka, *Dalton Trans.*, 2023, **52**, 13769–13780.

37 J.-H. Jeong, J. W. Park, D. W. Lee, R. H. Baughman and S. J. Kim, *Sci. Rep.*, 2019, **9**, 11271.

38 H. W. Nesbitt and D. Banerjee, *Am. Mineral.*, 1998, **83**, 305–315.

39 M. C. Biesinger, B. P. Payne, A. P. Grosvenor, L. W. M. Lau, A. R. Gerson and R. St C. Smart, *Appl. Surf. Sci.*, 2011, **257**, 2717–2730.

40 A. A. Audi and P. M. A. Sherwood, *Surf. Interface Anal.*, 2002, **33**, 274–282.

41 E. Turkusic, J. Kalcher, E. Kahrovic, N. W. Beyene, H. Moderegger, E. Sofic, S. Begic and K. Kalcher, *Talanta*, 2005, **65**, 559–564.

42 N. W. Beyene, P. Kotzian, K. Schachl, H. Alemu, E. Turkušić, A. Čopra, H. Moderegger, I. Švancara, K. Vytřas and K. Kalcher, *Talanta*, 2004, **64**, 1151–1159.

43 V. V. Poltavets, V. F. Vargalyuk, V. A. Seredyuk and L. V. Shevchenko, *J. Chem. Technol.*, 2018, **26**, 1–11.

44 J. Yang, R. Yu, W. Zhang, Y. Wang and Z. Deng, *Sensors*, 2025, **25**, 4132.

45 M. Jönsson-Niedziolka and V. Poltavets, 2026. RepOD, DOI: 10.18150/PUHR5I.